Ampere-class bright field emission cathode operated at 100 MV/m

Mitchell E. Schneider[1,2,3,*] Benjamin Sims,[1,2] Emily Jevarjian,[2] Ryo Shinohara,[1,2]
Tanvi Nikhar,[1] Taha Y. Posos,[1] Wanming Liu,[4] John Power,[4]
Jiahang Shao,[4] and Sergey V. Baryshev[1,†]

[1]*Department of Electrical and Computer Engineering, Michigan State University, Michigan 48824, USA*
[2]*Department of Physics and Astronomy, Michigan State University, East Lansing, Michigan 48824, USA*
[3]*Accelerator Operations and Technology Division, Los Alamos National Laboratory,*
Los Alamos, New Mexico 87545, USA
[4]*High Energy Physics Division, Argonne National Laboratory, Lemont, Illinois 60439, USA*

High-current bright sources are needed to power the next generation of compact rf and microwave systems. A major requirement is that such sources could be sustainably operated at high frequencies, well above 1 GHz, and high gradients, well above 100 MV/m. Field emission sources offer simplicity and scalability in a high-frequency era of the injector design, but the output rf cycle charge and high-gradient operation remain a great and largely unaddressed challenge. Here, a field emission cathode based on ultra-nano-crystalline diamond, an efficient planar field emission material, was tested at 100 MV/m in an *L*-band injector. A very high charge of 38 pC per rf cycle was demonstrated (300 nC per rf pulse corresponding to an rf pulse current of 120 mA). This operating condition revealed a two-dimensional space charge limited emission where the one-dimensional Child-Langmuir limit was surpassed. An injector brightness of 10^{14} A/(rad m)^2 was estimated for the given operating conditions.

I. INTRODUCTION

Rf injectors are the working horse electron guns producing relativistic electron beams finding ubiquitous applications in industrial, security, environmental, medical, and basic science sectors. The performance comparison can be drawn in terms of output current I, current density j, or beam brightness B, the latter of which is the most challenging and ambitious metric to achieve. Brightness is defined as $B = \frac{2I}{\varepsilon_\perp^2}$, where the total normalized transverse emittance $\varepsilon_\perp$ is found as $\varepsilon_\perp^2 = \varepsilon_{int}^2 + \varepsilon_{sc}^2 + \varepsilon_{rf}^2$ with ε_{int} being the intrinsic cathode emittance, and ε_{sc} and ε_{rf} being the space charge induced and rf induced emittance, respectively. The definitions of the brightness and emittance set the stage for rf injector developments. Such developments thus involve material science, emission physics, and high-power rf design. Additional sources of emittance growth exist due to electron optics not being ideal, e.g., astigmatic solenoid, but those can be fairly easily corrected by using a standard quadrupole-based stigmator [1,2].

With no special means, such as cathode surface topography [3], the space charge term is reduced through the increase of the macroscopic cathode rf field E (also termed gradient) as $\varepsilon_{sc} = \frac{1}{8} \frac{I}{I_A} \frac{\lambda}{\alpha} \frac{1}{3\frac{\sigma_\perp}{\sigma_z}+5}$, where I_A is the Alfven current of 17 kA, λ is the operating rf wavelength, $\sigma_\perp$ and σ_z are transverse and longitudinal bunch sizes, respectively, and $\alpha = \frac{eE}{4\pi m_e c^2}\lambda$ with m_e being the electron mass and c being the speed of light [4]. The development of high-frequency (*C*- to *W*- band) injectors is pivotal to greatly enhance the cathode peak electric field well above 100 MV/m to 300–500 MV/m, with 500 MV/m being demonstrated in *X*-band [5,6], as higher operating frequency greatly reduces the breakdown rate and simultaneously enhances the system compactness.

A trade-off here is that rf emittance grows with the gradient as $\varepsilon_{rf} = \frac{\sqrt{2}\pi^2}{\lambda^2} \frac{eE}{m_e c^2} \sigma_\perp^2 \sigma_z^2$ [7]. In the case of a photocathode, the rf emittance can be minimized by minimizing σ_z through the use of a phase matched femtosecond laser. In the case of *X*-band and higher frequencies [8], the use of a photocathode is extremely challenging due to size constraints, and another trade-off of using a field emission cathode (FEC) in place of photo emission technology must be evaluated in great detail. To enable FEC operation, special dc-ac or harmonic mixing gating

---

*schne525@msu.edu
†serbar@msu.edu

techniques or multicell designs were applied to reduce σ_z [7,9,10]. Since an injector that features high E and reduced σ_z has become available, it is critical to find a cathode material that (1) features low-intrinsic emittance, (2) is capable of emitting 1–100 pC per rf cycle (translating to a current of many Amperes), and yet (3) is capable of surviving when exposed to gradients on the order of 100 MV/m and above.

The present work extends our prior developments toward FEC-based high-frequency rf injector technology by utilizing ultra-nano-crystalline diamond (UNCD) as the cathode material. UNCD possesses exceptional emission efficiencies [11–14] and low-intrinsic emittance [15]. Diamond is a desirable material for high-power applications due to its thermal and mechanical properties. Despite this, diamond cathodes made in traditional high-aspect ratio geometries, such as pyramids [16,17], cannot offer high-gradient operation because they tend to explode at fields above 30–40 MV/m. Emission in diamond originates from sp^2 grain boundaries [18,19], and UNCD has the largest fraction of sp^2 phase as sp^3 grain size is the smallest among polycrystalline diamond. These are key factors that allow for simple planar FEC geometry with ~ 10 nm roughness and thus promise operation at high gradients near or above 100 MV/m. Therefore, this study simultaneously assesses (1) the survivability of UNCD up to 100 MV/m and its overall conditioning dynamics, (2) output charge per rf cycle under ultimate gradient conditions, (3) vacuum space charge-related effects, and (4) resulting beam brightness. The paper is laid out as the following: Section II describes the cathode fabrication; Section III describes the cathode testing facility; Section IV summarizes beam dynamics simulations and image processing approach; Section V summarizes conditioning procedure and cathode performance; Section VI provides discussion and physics implications; Section VII provides concluding remarks and outlook.

II. CATHODE FABRICATION

For this experiment, the UNCD cathode was grown on ultrasonically seeded molybdenum puck using microwave plasma-assisted chemical vapor deposition in a *S*-band reactor operated at 2.45 GHz [20,21]. A synthesis substrate temperature of 1248 K was achieved using a $H_2/(20\%)N_2/(5\%)CH_4$ feed gas mixture maintained at a flow rate of 200 standard cubic centimeters per minute (sccm) at a total gas pressure of 67.5 Torr and 3 kW microwave power. The substrate temperature was measured using an infrared pyrometer during the 1-h growth process. The UNCD coated puck was then mechanically attached to the three-part assembly, as outlined in Ref. [12]. Additionally, the edge of the cathode was carefully rounded, and UNCD coating covered the inner 18 mm of the 20 mm diameter puck to avoid edge effects.

The grown sample was then characterized using a Horiba Raman spectrometer with a 532 nm probing laser. The Raman spectrum typical to UNCD films illustrating D and G peaks centered around 1333 and 1560 cm^{-1}, respectively, were observed. This confirmed that the D peak corresponded to a high fraction of sp^3 diamond phase, and the G peak corresponded to semiamorphous sp^2 graphitic phases [20]. The deposition temperature was balanced such that the film exhibited high conductivity while still maintaining the sp^3 phase (shown by the presence of 1333 cm^{-1} peak). From experiments on insulating Si and quartz witness substrates, such a Raman corresponds to a resistivity of 0.5 $\Omega \cdot$ cm. High conductivity is likely due to improved crystallinity and physical connectivity between sp^2 grain boundaries as manifested by the G peak which is positioned at 1560 cm^{-1} [20]. Scanning electron microscopy (SEM) further confirmed the nanostructure typical of
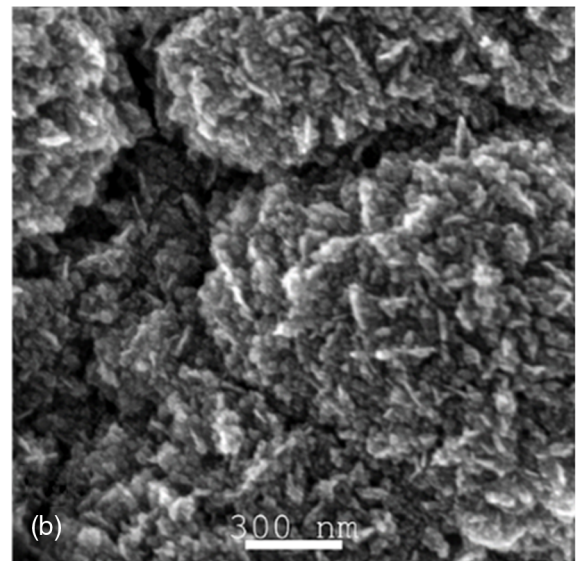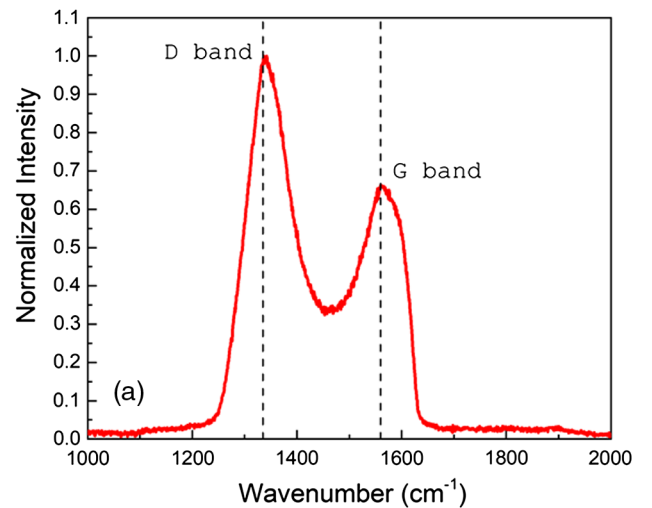

FIG. 1. Raman spectrum and SEM micrograph of as-grown sample.

UNCD. The summary of the Raman and SEM results are depicted in Fig. 1.

III. CATHODE TESTING FACILITY

The Argonne Cathode Teststand (ACT), an *L*-band (1.3 GHz) facility that is part of the Argonne Wakefield Accelerator (AWA) switchyard, was employed for testing the fabricated UNCD FEC and is depicted in Fig. 2. This operating frequency allows for larger dimension cathodes, higher charges, and improved imaging capabilities. From dc experiments [11,22], it is known that emission is nonuniform and nonmonotonic with the macroscopic electric field. Therefore, the ACT allows for extracting the charge and imaging the transverse emission profile to evaluate FEC performance and understand the underlying emission physics with the most detail possible.

The ACT injector is a single-cell normal conducting photoinjector [23] that is capable of operating in a pure field emission regime with the laser turned off. The repetition rate of the system is 2 Hz and the rf pulse length can be changed between 4 and 8 μs. The base vacuum pressure was maintained below 5×10^{-9} Torr. The ACTs rf system also has a bidirectional coupler which is used to measure the forward and reverse power.

The ACT has three solenoids along the beamline. The first two are the bucking and focusing solenoids which are coupled together such that the current runs in opposite directions in order to cancel out the axial magnetic fields inside of the gun. Additionally, the focusing solenoid has more windings than the bucking solenoid, allowing for focusing of the beam immediately after it exits the gun. This focusing primarily serves the purpose of increasing the capture ratio, and previous results seen in Ref. [12] have shown that this ratio can be optimized to well over 90% throughout conditioning.

In situ imaging is a unique feature of the ACT beamline: the third solenoid is the imaging solenoid, which is used to focus the beam for downstream imaging. To image the transverse electron distribution pattern, three Yttrium Aluminum Garnet (YAG) screens are used at different locations along the beamline. YAG1 is used to image the emission pattern as the beam exits the gun and can be interchanged with the Faraday cup. YAG3, located 2.54 m
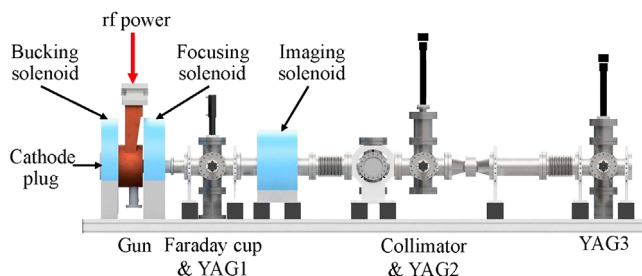
away from the cathode surface, is used to image the downstream on-axis electrons by the addition of a 1 mm aperture at the location of YAG2. Images on YAG2 allow for optimization of the solenoid settings to produce a beam waist at the location of YAG2, 1.55 m from the cathode.

Combining the imaging and image processing (using FEpic [24]), beam dynamics (using FEgen [25] paired with GPT [26]), and the charge and field measurements that are derived from the Faraday cup and bidirectional coupler (all done through a pipeline called FEbeam [27]) provides comprehensive analysis of the field emission cathode characteristics and performance.

IV. IMAGE PROCESSING AND BEAM DYNAMICS

Imaging was supported by beam dynamics simulations in GPT that were used to track an initial particle distribution generated in FEgen and a novel customized add-on for GPT that can convert any image file into an initial emission pattern on the cathode surface. The initial energy spread on the cathode surface was set to the intrinsic value of 0.1 eV, and the UNCD work function was assumed to be 4 eV from previous Kelvin probe measurements [28]. An initial pattern was produced using a field emission micrograph obtained for a UNCD cathode in dc (see Fig. 1 in Ref. [24]) and launched and captured at a time stamp corresponding to the YAG3 position. Figure 3(a) and 3(b) is a side-by-side comparison between the simulated and experimental emission imaging results at YAG3 which demonstrates a high degree of resemblance. From comparing simulations and imaging, emitters appear as bright stretched ellipses but not circular spots as seen in a dc case [11,22]. The emission spots are stretched along rays that start at the center of a cathode and go in all directions. They vary in length and brightness and are nonuniformly distributed in polar coordinates. Unlike in dc, electrons are generated by and interact with the rf or microwave drive cycle in a wide
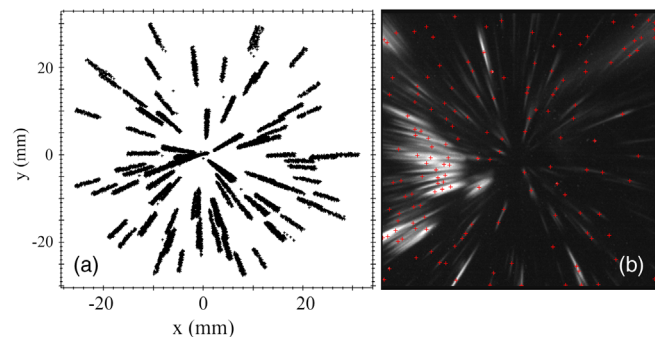

FIG. 3. Comparison of transverse electron patterns (a) as simulated in GPT and (b) as obtained experimentally, both at YAG3 position. The input emitter distribution was generated and imported using a pattern captured in dc, see Fig. 1 in Ref. [24]. Image (b) was processed with FEpic and counted emitters are labeled by red marks. All other images with local maxima identified and labeled as emitters can be found in the Appendix.

FIG. 2. Schematic of the ACT beamline.

phase window. The extended interaction phase window causes the ellipses (or streaks) to form and are essentially represented as rotated projections of longitudinally stretched electron beamlets arriving from the cathode surface. At this distance from the gun, the spatiotemporal behavior of the beam is dominated by rf emittance ε_{rf}. It can be concluded that each line represents a singular emitter and that counting the streaks should be representative of the number of emitters and their variation as a function of the external power in the rf injector.

Charge and image collection were conducted hand in hand at different gradients. The images were processed using FEpic to obtain the emitter population statistics throughout the FEC conditioning process. In brief, FEpic partitions the image into equal sections and then finds brightest pixels in each of those sections. Then, it utilizes a so-called decision plot that relates the intensity of a brightest pixel and the distance between this pixel and its closest neighbor. It then applies a special filter to sort emission centers from glowing background or dead pixels. Figure 3 shows an exemplary calculation of the number of emitters and the full set of image processing results can be found in Appendix.

V. FEC PERFORMANCE

Based on the previously developed methodology for high-power conditioning [12], the UNCD FEC was continuously conditioned from a turn-on field, determined to be 9 MV/m all the way up to 100 MV/m in increments of 5 MV/m. 9 MV/m was pinpointed to be the turn-on field as the electron emission signal was first detected on YAG1 at this field, though the charge on the Faraday cup was below the detection limit.

QvsE curves were taken as follows. Each conditioning field was taken in 5 MV/m increments and the gradient was increased until each conditioning field, E_h, was achieved. The system was maintained at a given E_h until the breakdown rate reduced to $\sim 10^{-4}$ per pulse. Every QvsE curve was then taken with decreasing increments of 0.5 MV/m until the point where no charge was detected by the Faraday cup.

The first experimental session could not go above 70 MV/m as a breakdown event with a breakdown rate spiked instantaneously exceeding 10^{-1} per pulse. This occurred when the cathode was attempted to be run at 75 MV/m for data collection. Therefore, the first session was concluded and a second session had to be carried out after the breakdown source was identified and addressed. Upon stopping the experiment, the as-installed cathode was optically viewed inside the gun, allowing for the breakdown source to be identified as a single location on the uncoated rounded molybdenum puck edge. The inset in Fig. 4 shows the outer edge as a light blue circle and the breakdown location can be seen as a light blue thick dot located at 1 o'clock. The entire UNCD surface was
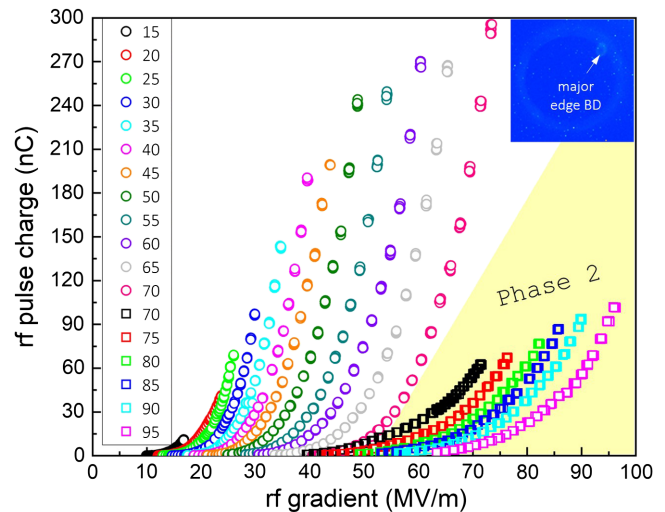

FIG. 4. The QvsE curves for Phases 1 and 2 separated into two regions corresponding to the experiment runs. In the legend, the numerical values label the maximum conditioning gradient achieved per QvsE curve (referred to as E_h). The inset shows an *in situ* taken image of the major breakdown event, located on the outer edge of the cathode puck at 1 o'clock (labeled with an arrow), that stopped the Phase 1 session.

determined to be unharmed by this major breakdown event. The FEC edge was refinished, and the FEC was reinserted into the gun for the second experimental session, demonstrating an additional extent of the UNCD FEC endurance capabilities.

During the second phase, the cathode was conditioned back up to 70 MV/m in a matter of 2 h with only three breakdowns occurring during the entire process. QvsE curves were then taken from 70 to 95 MV/m in the same manner as was done in the first phase. 96 ± 4 MV/m was the maximum achievable field due to power limited output of the klystron. Figure 4 highlights that the output charge remained at the same order of magnitude of 100 nC despite the reinstallation process that involved micromachining and air exposure. Additionally, Phase 2 experiments showed the steady increase of the output charge with increasing gradient. This is an impressive result for an rf injector where a FEC produced 0.1 A of current at 100 MV/m. Figure 5 compares emission patterns captured at 70 MV/m before and after the Phase 1 experiments stopped and restarted in Phase 2. One can see that the reduced output charge is a consequence of the reduced emission area. The exact reason behind the drop in charge (and apparent emission area) remains unknown and requires designed experiments where the conditioning process must be interrupted and the cathode reinstalled and reconditioned again such that QvsE curves and images are continuously recorded. Furthermore, it is clear from Fig. 5 that the family of emitters that dominated the emission in Phase 1 are the same emitters producing charge in Phase 2. It should be noted that, in the ACT gun, there is no locking mechanism
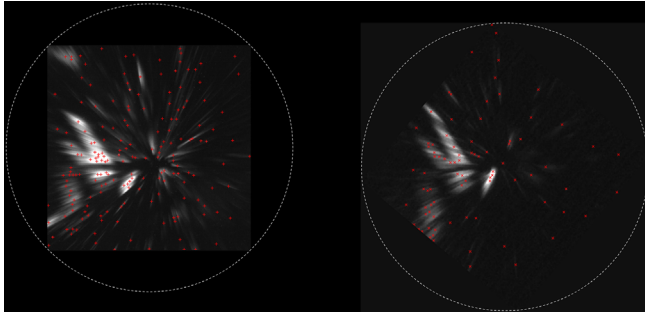
FIG. 5. Comparison between emission patterns on YAG3 at 70 MV/m taken in Phases 1 (left) and 2 (right, rotated CCW by 50 deg). The images are placed with respect to the origin: since there is slight y offset in the left image, the right rotated image rests below against the left image.

when installing a cathode. During reinstallation, the cathode was unintentionally rotated by 50 deg, as was determined from matching the major emission cluster on the right side of the images taken at 70 MV/m.

Raw data analysis and conversion to QvsE curves, as well as plotting and analysis in various coordinates, was accomplished using a data processing pipeline called FEbeam which is described in a great detail in Ref. [27]. FEbeam begins by taking the raw voltage signal waveforms for the diodes measuring forward power, reverse power, and Faraday cup to calculate the QvsE curves. These are then translated into Fowler-Nordheim coordinates by analyzing the rf drive signal envelope and finding its temporal structure. The rf pulse length was 6 μs throughout the presented experiments. This resulted in a constant scaling factor when plotting either QvsE or IvsE curves where I is the rf pulse current. As before, Fowler-Nordheim coordinates for the rf case are $\log_{10}(\frac{\bar{I}}{E^{2.5}})$ vs $(\frac{1}{E})$ [29] as per the modified, time-averaged Fowler-Nordheim relation:

$$\overline{I_F(t)} = \frac{5.7 \times 10^{-12} \times 10^{4.52\phi^{-0.5}} A_e [\beta|E_c(t)|]^{2.5}}{\phi^{1.75}}$$
$$\times \exp\left[-\frac{6.53 \times 10^9 \phi^{1.5}}{\beta|E_c(t)|}\right]. \qquad (1)$$

Unlike in previous rf cases [12,14], a significant divergence from classical Fowler-Nordheim (FN) law was revealed, which is obviously the result of the exceptionally high charge despite the duty cycle being extremely low, namely 6×10^{-6} at 1 Hz. The divergence is manifested by the presence of the knee point (previously discussed for a dc case elsewhere [22]): two linear fits of a different slope exist intersecting at the knee point. Due to the large gradient incremental step (and thus, a smaller number of data points), a new automated algorithm to retrieve the knee point was implemented in FEbeam. The algorithm determines the knee point location along with the relative ranges of the R^2 values of the iterative fitting for the line segments
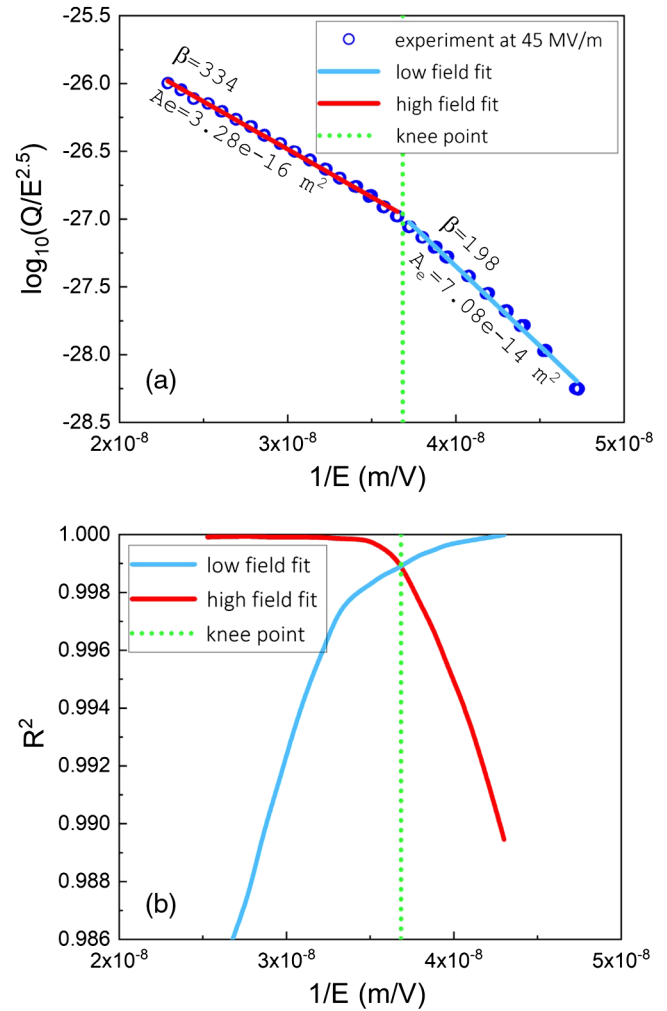

FIG. 6. (a) FN plot and (b) R^2 plot exampled for 45 MV/m. Here, E stands for rf gradient.

as depicted in Fig. 6. Here, R^2 represents the goodness of the linear fit.

After the knee point is selected, FEbeam performs FN fitting to two linear portions, separated by the knee point, in FN coordinates. Therefore, there are low-gradient and high-gradient portions of QvsE dependencies. For both portions, FEbeam then extracts the field enhancement factor (β), the local field on the cathode surface ($\beta \times E_h$), and the effective emission area (A_e), all as a function of the maximum achieved conditioning field (E_h) per formalism below [12],

$$\begin{cases} \beta = \frac{-2.84 \times 10^9 \phi^{1.5}}{s} \\ A_e = \frac{10^{y_0} \phi^{1.75}}{5.7 \times 10^{-12} \times 10^{4.52\phi^{-0.5}} \beta} \\ E_L = \beta \times E_h, \end{cases} \qquad (2)$$

where s and y_0 are the slope and the y axis intercept of the linear dependence, and ϕ is the work function. The result summary is presented in Fig. 7.
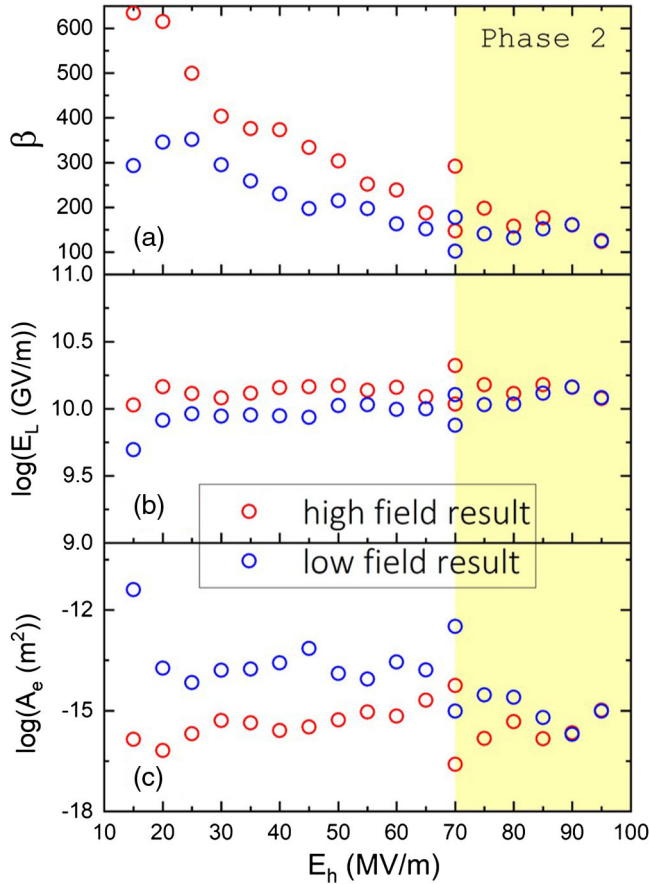
FIG. 7.   Field emission conditioning parameters: (a) field enhancement factor, (b) local field on the cathode surface, and (c) effective emission area for both the FN-like (low field) and non-FN (high field) regions.

High-field data resulted in an overestimation of the local field, as it is known that a local field above 10 GV/m may be nonphysical due to exceeding the limit set by the lattice interatomic force. This value includes diamond that breaks down at ∼10 GV/m [30]. Experimentally, this would likely result in an immediate failure of the cathode due to breakdown induced runaway of the cathode material [31,32]. Since the cathode was not observed to behave in this way, it was concluded that high-field data overestimates the field enhancement factor. In contrast, the low-field data predicted the local field to be at or below 10 GV/m. None of the datasets predicted the emission area correctly either in its magnitude or with respect to the gradient trend. Though incorrect, the effective emission area for the low-field portion decreases with E_h which is in agreement with classical FN law [22]. The high-field portion predicts the effective emission area to be a nearly constant value. Therefore, the low-gradient portion can be attributed to the classical metal-like FN behavior, while the high-gradient portion is driven by a different physical mechanism which is discussed further.

VI. LEADING HYPOTHESIS AND DISCUSSION

Generally, there are two competing hypotheses to explain deviation from classical FN behavior of planar FECs (when charge grows slower than predicted by FN law). One is space charge limited emission [33,34]. In this case, if an extensive charge is emitted and not removed away from the cathode's surface promptly, it may start screening the external electric field—hence, the emission curve diverges from the FN trend. The second of the competing hypotheses is based on resistance limited emission: in the 1960s, it was discovered that semiconductor and semimetal field emitters do not obey FN law. In experiments, the output current stops growing with the electric field and current-voltage characteristics switch from diode-like to resistor-like behavior. The ballast, or series resistance forcing the diode-to-resistor transition to take place, can be caused by the contact resistance [35] or by the transit time limited resupply of limited amount of charge being emitted through the limited amount of emission spots on the surface of the cathode [22,36,37]. Our leading hypothesis is that it is space charge that affects the emission and causes the observed divergence from classical FN in this particular study. This is supported by a series of the following observations.

All measurements were taken in fields stronger than 10^4 V/cm. This means that, at all gradients, charge drift can be expected to be saturated [36]. The number of emitters quickly increased and remained near a constant value as obtained by *in situ* imaging at E_h for every conditioning QvsE curve. For the purpose of this analysis, we were interested in the downstream imaging using YAG3 images as it enables the largest magnification and resolution (when coupled with the collimator at the YAG2 position). To achieve high-resolution dark current imaging, a method to select electrons from certain emitting phases and narrow the energy spread was developed using external axial magnetic fields (i.e., solenoids) and a collimator at the focal plane, as is discussed in more detail in Ref. [38]. The resolution improves when smaller apertures are imposed. There is a trade-off between the resolution and the signal-to-noise. The standard technique is to apply a 1 mm aperture—it enables strong signal and resolution of 100 μm. All imaging was carried out using a metal collimator with an on axis centered circular aperture of 1 mm in diameter. The number of emitters (or local maxima, in terms of image processing terminology) on the cathode surface was determined by processing a set of 18 raw 16-bit images using FEpic [24] shown in Appendix A in their entirety.

Each emitter that was determined to be present through image processing was assumed to have had the same area such that the total emission area was the number of emitters times the unit emitter area. The charge growth at every E_h point slowed down but did not plateau out on the semilog
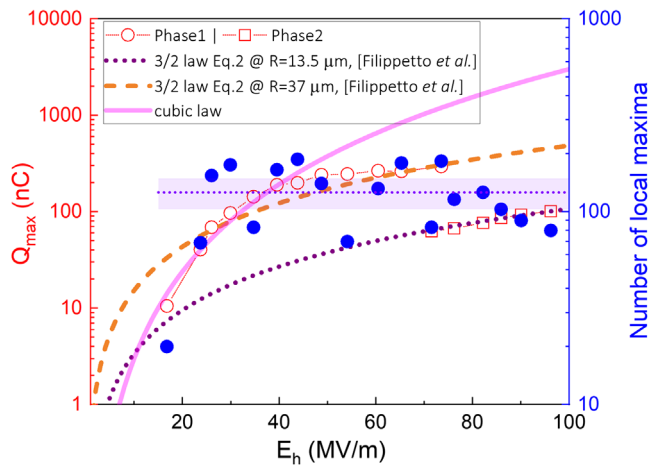
FIG. 8. Maximum charge and the number of emitters determined at the maximum of every conditioning QvsE curve as functions of E_h. The purple horizontal area represents one standard deviation around the mean value of the emitter number count.

plot as it would be expected to based on the series resistor model. This confirms the leading role of the electric field effects outside (and not inside) the cathode. Figure 8 sums up this representation by illustrating that the charge dynamics are driven by the electric field and not the emitter statistics (given the charge drift transport in UNCD bulk must be considered saturated at all gradients [36]). To further elaborate on these conclusions, we utilize two-dimensional (2D) space charge formalism developed by Filippetto *et al.* elsewhere [39]. Having a field emission period of 38 ps in L-band, the generated beam can be termed as the cigar aspect ratio beam. Therefore, the 2D space charge formalism fully applies. Specifically, the following equation is used to fit Q_{max} vs E_h dependencies

$$Q_{max}^{2D} = C_c I_A \frac{\sqrt{2}}{9} \left(\frac{eE_hR}{mc^2} \right)^{3/2} \Delta t, \qquad (3)$$

where C_c is an order-of-unity constant, R is the emission radius, and Δt is the emission period equal to 38 ps.

The Phase 2 dependence was fit very well by Eq. (3) (purple dotted line and red square symbols) and an emission area radius of 13 μm was obtained (all other parameters were fixed). These results present direct evidence of the 2D space charge limited emission. In Phase 1, the last three gradient points (60, 65, and 70 MV/m) were fit well by Eq. (3) (orange dashed line and red circle symbols), yielding an emission area radius of 37 μm. The gradients between 15 and 40 MV/m were fit well by a cubic law which Eq. (3) becomes if the gradient and emission radius are both changing at the same time. This assumption is supported by the imaging results plotted on the same graph illustrating and confirming the validity of

cubic law application in this gradient range. While the gradient is changing from 15 to 40 MV/m, the emission radius is changing from 18 to 44 μm. The transition between 3 and 3/2 laws occurred between 40 and 60 MV/m and is not well captured in our experiments. The difference between extracted emission radii, 37 down to 13 μm, is consistent with the result seen in imaging: even though the main emission pattern remained after cathode reinstallation, the number of streaks (i.e., number of localized emitters) dropped. Equation (3) estimates this drop to be by a factor of 3. This is, again, consistent with the image processing algorithm results that predicted a relative drop of the number of emitters by a factor of 2. Two observations are worth noting here: First, the emission area extracted from Eq. (3) is six orders of magnitude larger than that predicted from FN fitting as is depicted in Fig. 7. Second, the space charge limited emission appears a better regime to extract the field emission area. The same phenomenon was observed in the transit time limited emission [37] which predicts a saturation in the effective emission area that resembles a more realistic observable field emission area as is supported by our image processing results.

Combining the field emission QvsE characteristics with the emitter statistics presents clear evidence that the divergence from the classical FN regime is a result of space charge limited field emission. Confirmation that the emitter count is approximately constant while the charge grows as a function of E_h shows that the charge density is still growing throughout conditioning, though at a slower rate. The difference between the one-dimensional (1D) Child-Langmuir law and 2D space charge limited emission, resulting from elongated beam due to a long launch phase window, is reinforced by the Millikan plot
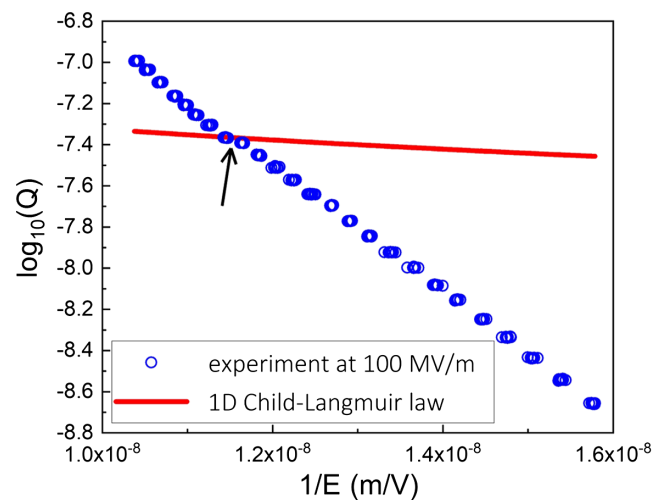

FIG. 9. Millikan plot for 100 MV/m (blue circles) showing the parallel shift denoted with an arrow and is indicative of a space charge dominated regime that differs from the Child Langmuir law (red line). Here, E stands for rf gradient.

(a better way to visualize the space charge onset [34]) corresponding to 100 MV/m, as shown in Fig. 9: the charge surpassed what the Child Langmuir limit predicts. A small parallel shift can be observed which is indicative of switching to space charge limited emission for high work function materials (>3.5 eV) [34]. In our experiment, the 1D limit was surpassed by a factor of 2. In a different version of a 2D space charge case, Luginsland *et al.* [40] demonstrated how the Child-Langmuir problem considered in two-dimension led to surpassing the classical 1D law of 2/3: 2D current was higher than 1D current by a factor of 4.

Finally, we used the estimated effective emission radii (37 μm in Phase 1 at 70 MV/m and 13 μm in Phase 2 at

100 MV/m) obtained from Eq. (3) and corresponding charges per rf cycle (38 pC in Phase 1 at 70 MV/m and 13 pC in Phase 2 at 100 MV/m) to track the brightness evolution from the cathode surface to the gun exit and down the beamline all the way to YAG3. The summary plots in Fig. 10 include all the emittance components used in the brightness evaluations, namely space charge, intrinsic and rf emittances. The intrinsic emittance was evaluated from a previously measured mean transverse energy value of 100–200 meV [15]. The presented end-to-end beam tracking results further reinforce that, in the gun, the beam is dominated by the space charge force leading the transverse brightness to settle at approximately 10^{14} A/(rad m)^2, the gun brightness in both
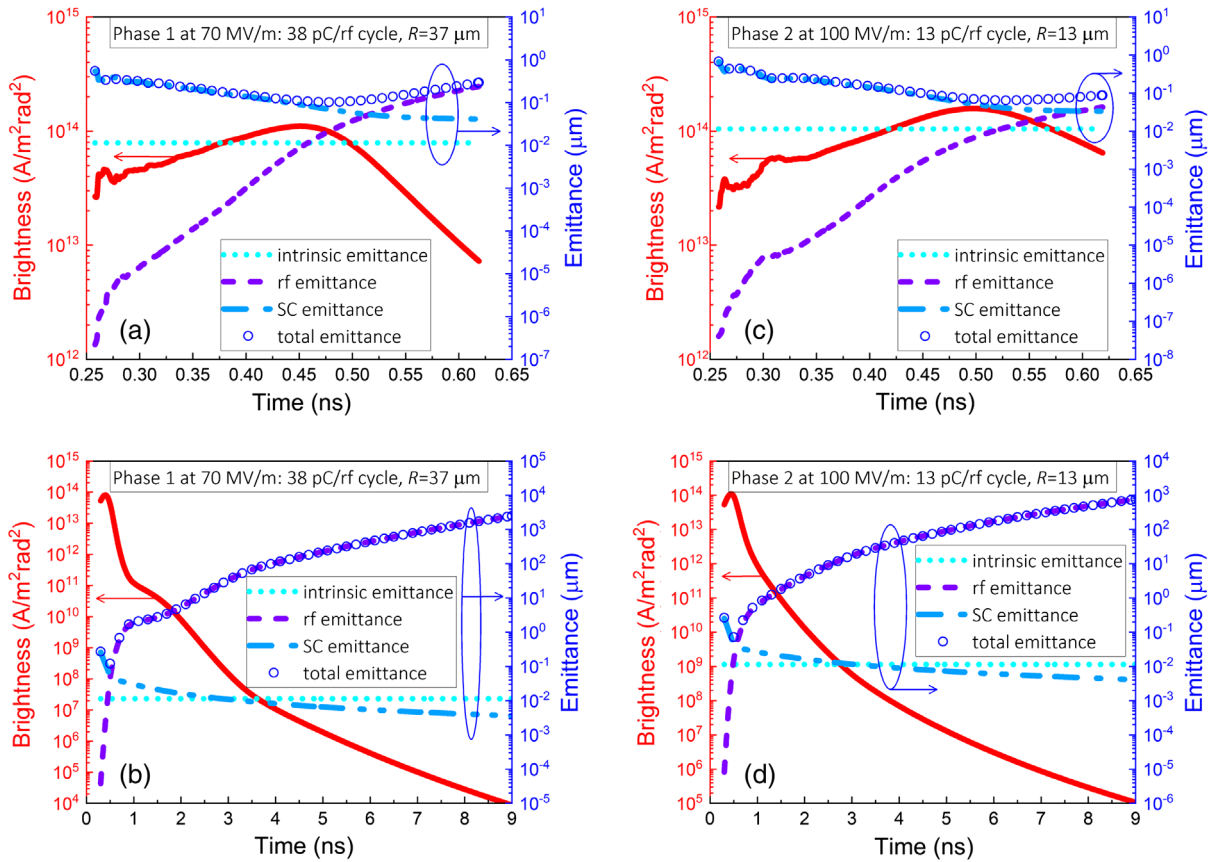

FIG. 10. Brightness dynamics inside the gun for (a) Phase 1 and (c) Phase 2 and along the entire beamline from the cathode to YAG3 for (b) Phase 1 and (d) Phase 2. For reference, the gun exit corresponds to the time stamp of 0.45 ns for all the figures.

Phases 1 and 2. Outside the gun, from 1 to 9 ns, the rf emittance takes over due to longitudinal beam stretching caused by the launch phase effect. With this drift to YAG3, the brightness quickly dropped to insignificant values. As stated before, this rf emittance growth is responsible for the YAG3 image streaking.

The analytical calculations using the formalism presented in the introduction section predict the gun brightness of $\sim 10^{14}$ A/(rad m)^2 which is close to the exact metrics found in GPT. The same formalism suggests that suppressing the temporal emission window to a few or sub-picoseconds would minimize the dominating factor of rf emittance within the drift space. Additionally, still by the same formalism, enabling cathode gradients between 300 and 500 MV/m could provide a practical path toward brightness well above 10^{15} or near 10^{16} A/(rad m)^2 for a C- or X-band injector family, which would be a technological breakthrough. Some practical techniques for longitudinal suppression are (1) direct gating or frequency mixing in the gun [9], (2) obtaining a specialty multicell gun design [41], or compressing the beam with either (3) an external TM_{10} cavity [42], or (4) a self-wakefield structure followed by ballistic bunching or chicane lensing [43]. While offering injector simplicity over photocathodes especially in high-frequency systems, field emitters would be electron sources of choice for many applications if a certain level of coherent beams can be experimentally proven. The validity of these FECs will require knowledge of the interplay between the emitted charge and the emission area and, therefore, would require a detailed study. In this case, operation using planar field emitter geometries is required to avoid physical disruption of the cathode.

VII. CONCLUSION AND OUTLOOK

An ultra-nano-crystalline diamond FEC was operated at 100 MV/m in L-band in the newly established 2D space charge regime. A charge of 100–300 nC per rf pulse (13–38 pC per rf cycle) was demonstrated. Output gun brightness of 10^{14} A/(rad m)^2 was estimated for the given experimental conditions, and brightness between 10^{15} and 10^{16} A/(rad m)^2 is anticipated as a practical benchmark with further improvements of operating gradient in C- to X-band injector designs. UNCD conditioning and stability analysis moving toward 300–500 MV/m operation is the next step necessary to extend its application.
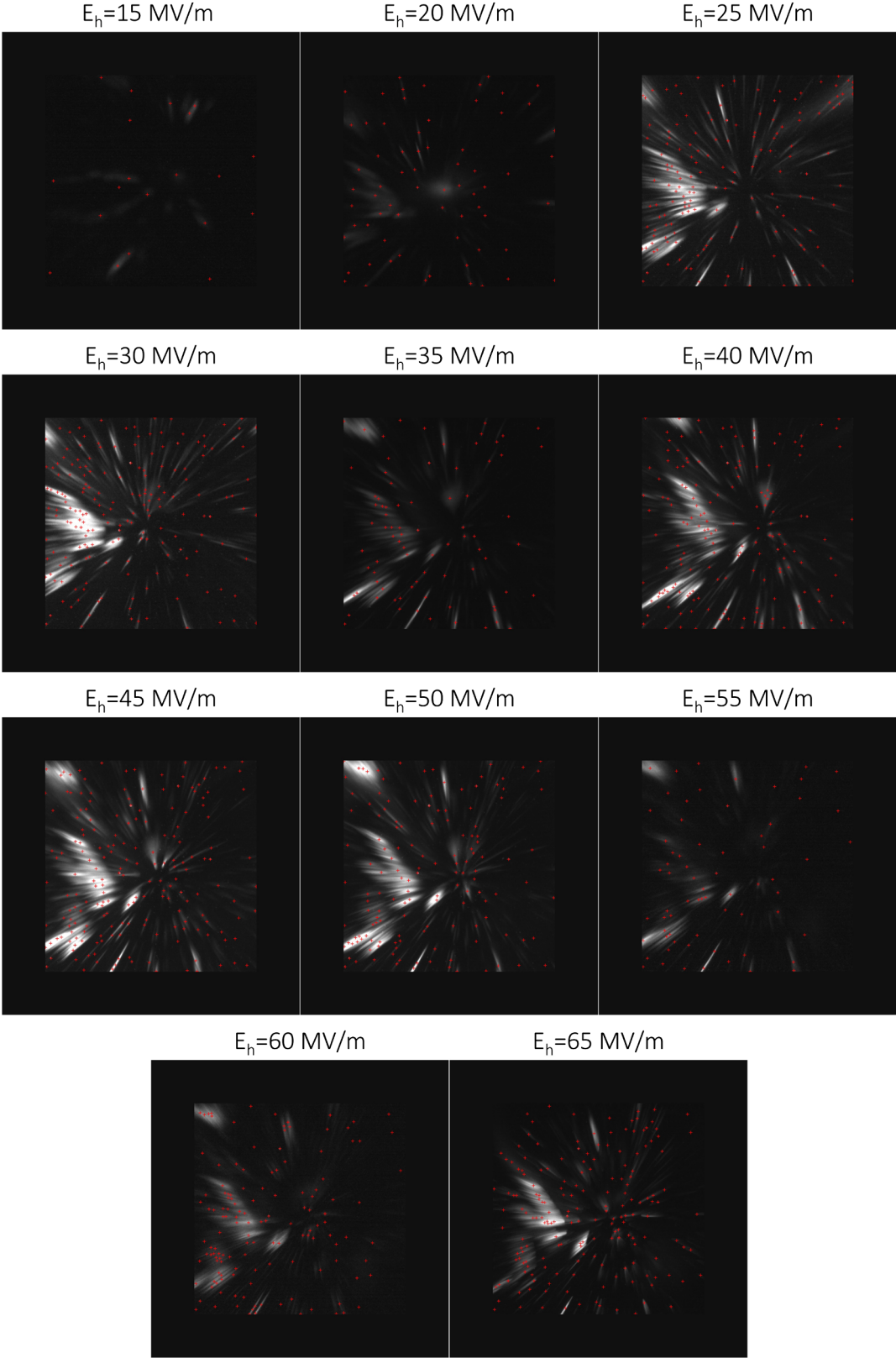
Further exploration and parametrization, in terms of the boundaries of charge and field, of the space charge limited emission regime is underway. Immense gradient values enabled by microwave injectors, where effective voltages of 2 MV or more can be applied, allow for looking well beyond the physics of both Fowler-Nordheim and Child-Langmuir, an extremely challenging endeavor with pulsed dc systems. Comparisons of planar vs nonplanar geometries with high-aspect ratios should provide insight into the interplay between gradient and charge density effects in space charge limited emission. In turn, understanding this new regime of field emission physics is crucial for informed improvement of the next generation of sources and injectors.
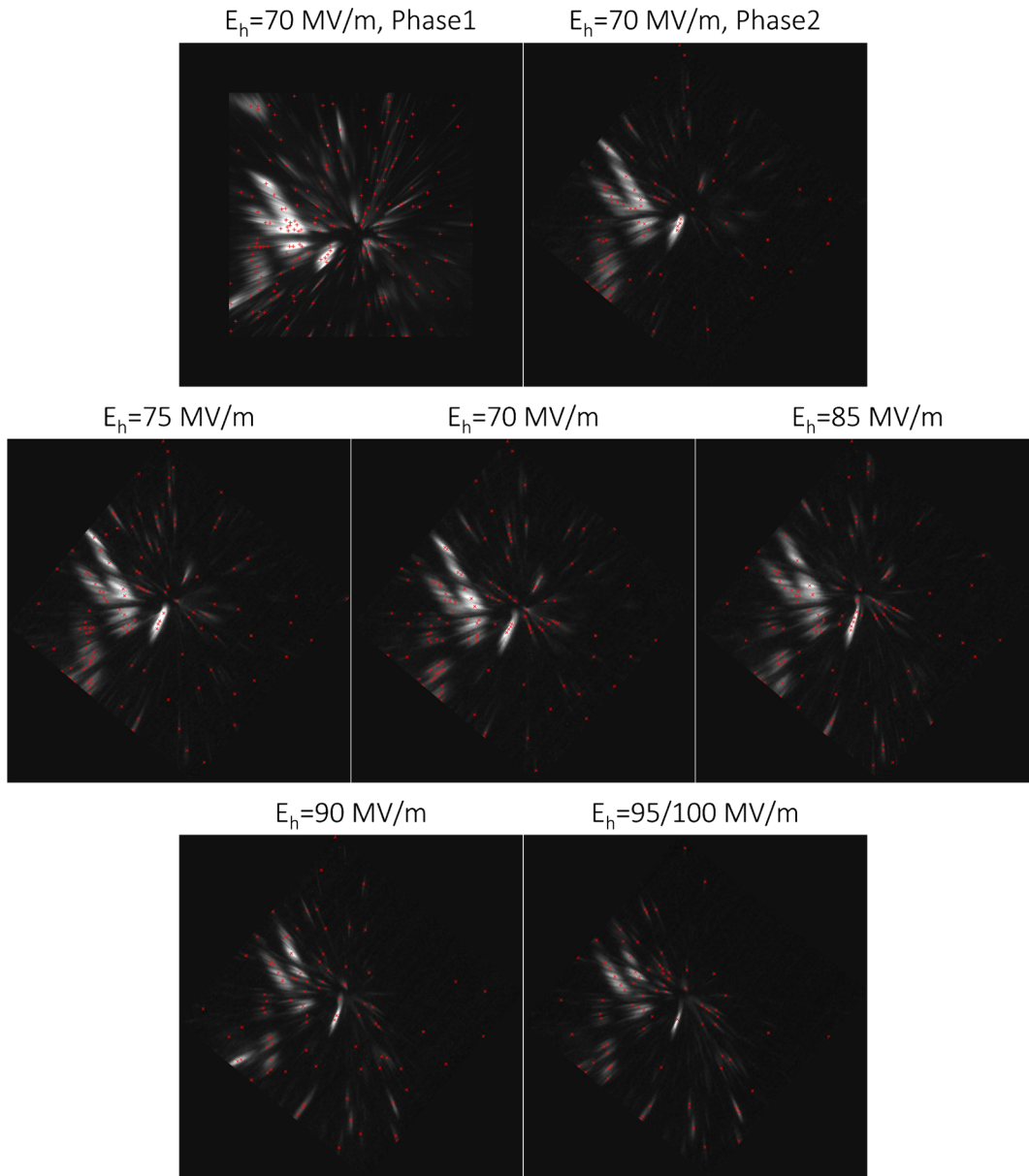
APPENDIX: RF MICROSCOPY: EXPERIMENTALLY COLLECTED IMAGES PROCESSED IN FEPIC

Shown here are processed images indicating local maxima with red markers.

E_h=15 MV/m E_h=20 MV/m E_h=25 MV/m

E_h=30 MV/m E_h=35 MV/m E_h=40 MV/m

E_h=45 MV/m E_h=50 MV/m E_h=55 MV/m

E_h=60 MV/m E_h=65 MV/m

E_h=70 MV/m, Phase1

E_h=70 MV/m, Phase2

E_h=75 MV/m

E_h=70 MV/m

E_h=85 MV/m

E_h=90 MV/m

E_h=95/100 MV/m

[1] L. Zheng, J. Shao, Y. Du, J. G. Power, E. E. Wisniewski, W. Liu, C. E. Whiteford, M. Conde, S. Doran, C. Jing, C. Tang, and W. Gai, Phys. Rev. Accel. Beams **22**, 072805 (2019).

[2] J. Qiu, G. Ha, C. Jing, S. V. Baryshev, B. W. Reed, J. W. Lau, and Y. Zhu, Ultramicroscopy **161**, 130 (2016).

[3] D. H. Dowell, Phys. Rev. Accel. Beams **22**, 084201 (2019).

[4] K.-J. Kim, Nucl. Instrum. Methods Phys. Res., Sect. A **275**, 201 (1989).

[5] A. D. Cahill, J. B. Rosenzweig, V. A. Dolgashev, S. G. Tantawi, and S. Weathersby, Phys. Rev. Accel. Beams **21**, 102002 (2018).

[6] V. Dolgashev, S. Tantawi, Y. Higashi, and B. Spataro, Appl. Phys. Lett. **97**, 171501 (2010).

[7] L. Schchter, W. D. Kimura, and I. Ben-Zvi, AIP Conf. Proc. **1777**, 080013 (2016).

[8] M. A. K. Othman, J. Picard, S. Schaub, V. A. Dolgashev, S. M. Lewis, J. Neilson, A. Haase, S. Jawla, B. Spataro, R. J. Temkin, S. Tantawi, and E. A. Nanni, Appl. Phys. Lett. **117**, 073502 (2020).

[9] J. W. Lewellen and J. Noonan, Phys. Rev. ST Accel. Beams **8**, 033502 (2005).

[10] X. Li, M. Li, L. Dan, Y. Liu, and C. Tang, Phys. Rev. ST Accel. Beams **16**, 123401 (2013).

[11] O. Chubenko, S. S. Baturin, K. K. Kovi, A. V. Sumant, and S. V. Baryshev, ACS Appl. Mater. Interfaces **9**, 33229 (2017).

[12] J. Shao, M. Schneider, G. Chen, T. Nikhar, K. K. Kovi, L. Spentzouris, E. Wisniewski, J. Power, M. Conde, W. Liu,

and S. V. Baryshev, Phys. Rev. Accel. Beams **22**, 123402 (2019).

[13] S. V. Baryshev, S. Antipov, J. Shao, C. Jing, K. J. P. Quintero, J. Qiu, W. Liu, W. Gai, A. D. Kanareykin, and A. V. Sumant, Appl. Phys. Lett. **105**, 203505 (2014).

[14] S. V. Baryshev, E. Wang, C. Jing, V. Jabotinski, S. Antipov, A. D. Kanareykin, S. Belomestnykh, I. Ben-Zvi, L. Chen, Q. Wu, H. Li, and A. V. Sumant, Appl. Phys. Lett. **118**, 053505 (2021).

[15] T. Nikhar, S. V. Baryshev, G. Adhikari, and A. W. Schroeder, arXiv:2011.00722.

[16] H. Andrews, K. Nichols, D. Kim, E. I. Simakov, S. Antipov, G. Chen, M. Conde, D. Doran, G. Ha, W. Liu, J. Power, J. Shao, and E. Wisniewski, IEEE Trans. Plasma Sci. **48**, 2671 (2020).

[17] K. E. Nichols, H. L. Andrews, D. Kim, E. I. Simakov, M. Conde, D. S. Doran, G. Ha, W. Liu, J. F. Power, J. Shao, C. Whiteford, E. E. Wisniewski, S. P. Antipov, and G. Chen, Appl. Phys. Lett. **116**, 023502 (2020).

[18] R. L. Harniman, O. J. Fox, W. Janssen, S. Drijkoningen, K. Haenen, and P. W. May, Carbon **94**, 386 (2015).

[19] J. B. Cui, J. Ristein, and L. Ley, Phys. Rev. B **60**, 16135 (1999).

[20] T. Nikhar, R. Rechenberg, M. F. Becker, and S. V. Baryshev, J. Appl. Phys. **128**, 235305 (2020).

[21] J. Asmussen, T. A. Grotjohn, and T. Schuelke, in *Ultananocrystalline Diamond (Second Edition)* (William Andrew Publishing, Oxford, 2012), pp. 53–83.

[22] T. Y. Posos, S. B. Fairchild, J. Park, and S. V. Baryshev, J. Vac. Sci. Technol. B **38**, 024006 (2020).

[23] C. H. Ho, T. T. Yang, J. Y. Hwang, G. Y. Hsiung, S. Y. Ho, M. C. Lin, M. Conde, W. Gai, R. Konecny, J. Power, and P. Schoessow, SRRC/ANL High Current L-band Single Cell Photocathode RF Gun, Technical Report (PAC Proceedings TU33C, 1441, 1998).

[24] T. Y. Posos, O. Chubenko, and S. V. Baryshev, arXiv:2012.03578.

[25] E. Jevarjian, M. Schneider, and S. V. Baryshev, arXiv:2009.13046.

[26] S. van der Geer and M. de Loos, *General Particle Tracer* (Pulsar Physics), http://pulsar.nl/.

[27] M. Schneider, E. Jevarjian, J. Shao, and S. V. Baryshev, Rev. Sci. Instrum. **92**, 053305 (2021).

[28] G. Chen, G. Adhikari, L. Spentzouris, K. K. Kovi, S. Antipov, C. Jing, W. A. Schroeder, and S. V. Baryshev, Appl. Phys. Lett. **114**, 093103 (2019).

[29] J. Wang and G. Loew, Field emission and rf breakdown in high-gradient room temperature linac structures, Technical Report (Stanford Linear Accelerator Center, 1997), https://www.slac.stanford.edu/pubs/slacpubs/7500/slac-pub-7684.pdf.

[30] A. Hiraiwa and H. Kawarada, J. Appl. Phys. **114**, 034506 (2013).

[31] A. Kyritsakis, M. Veske, K. Eimre, V. Zadin, and F. Djurabekova, J. Phys. D **51**, 225203 (2018).

[32] S. S. Baturin, T. Nikhar, and S. V. Baryshev, J. Phys. D **52**, 325301 (2019).

[33] J. W. Luginsland, A. Valfells, and Y. Y. Lau, Appl. Phys. Lett. **69**, 2770 (1996).

[34] J. P. Barbour, W. W. Dolan, J. K. Trolan, E. E. Martin, and W. P. Dyke, Phys. Rev. **92**, 45 (1953).

[35] P. Zhang, S. B. Fairchild, T. C. Back, and Y. Luo, AIP Adv. **7**, 125203 (2017).

[36] O. Chubenko, S. S. Baturin, and S. V. Baryshev, J. Appl. Phys. **125**, 205303 (2019).

[37] T. Y. Posos, O. Chubenko, and S. V. Baryshev, ACS Appl. Electron. Mater. **3**, 4990 (2021).

[38] J. Shao, J. Shi, S. P. Antipov, S. V. Baryshev, H. Chen, M. Conde, W. Gai, G. Ha, C. Jing, F. Wang, and E. Wisniewski, Phys. Rev. Lett. **117**, 084801 (2016).

[39] D. Filippetto, P. Musumeci, M. Zolotorev, and G. Stupakov, Phys. Rev. ST Accel. Beams **17**, 024201 (2014).

[40] J. W. Luginsland, Y. Y. Lau, and R. M. Gilgenbach, Phys. Rev. Lett. **77**, 4668 (1996).

[41] X. Li, M. Li, L. Dan, Y. Liu, and C. Tang, Phys. Rev. ST Accel. Beams **16**, 123401 (2013).

[42] T. van Oudheusden, P. L. E. M. Pasmans, S. B. van der Geer, M. J. de Loos, M. J. van der Wiel, and O. J. Luiten, Phys. Rev. Lett. **105**, 264801 (2010).

[43] F. Lemery and P. Piot, Phys. Rev. ST Accel. Beams **17**, 112804 (2014).